Induced EM Field in a Layered Eccentric Spheres Model of the Head: Plane-Wave and Localized Source Exposure

Nikos C. Skaropoulos, *Student Member, IEEE,* Melina P. Ioannidou, *Student Member, IEEE,* and Dimitris P. Chrissoulidis, *Member, IEEE*

Abstract— **The induced electromagnetic (EM) field in a layered eccentric spheres structure is determined through a concise analytical formulation based on indirect mode-matching (IMM). The exact analytical solution is applied to a six-layer model of the head. This model allows for eccentricity between the inner and outer sets of concentric spherical layers which simulate brain and skull, respectively. Excitation is provided by a nearby localized source or by an incident plane wave. The numerical application provides information about the total absorbed power, the absorption in each layer, and the spatial distribution of the specific absorption rate (SAR) at frequencies used by cellular phones. The effects of excitation frequency, eccentricity, exposure configuration, and antenna-head separation are investigated.**

I. Introduction

UNDERSTANDING the interaction of EM radiation with humans is essential in a number of contemporary applications. There is currently strong interest in the biological effects and in the medical use of radio-frequency (RF) and microwave radiation [1]. Special attention is paid to the absorption of EM energy by the human head, which exhibits a resonant behavior in the frequency band 0.1–3 GHz. The use of handheld transceivers for wireless communications, which operate in close proximity to the head, has raised safety-related questions and questions concerning the effect of the head on the performance of the mobile phone antenna.

Research on the induced EM field in the human head is aimed at determining the total absorbed power and the SAR distribution [1]. Calculations are mostly performed by numerical techniques which can be applied to complex, hence realistic, geometries. Analytical techniques necessarily deal with simpler head/exposure models. Nevertheless, analytical solutions are useful for synoptic surveys of the interaction of EM radiation with the human head and they are indispensable as benchmarks for numerical solutions.

Primary numerical efforts to determine the SAR distribution in the human head were based on the finite-element method (FEM) [2]. Lately, interest has been focused on the finite-difference time-domain (FDTD) method which was used in conjunction with anatomically realistic head models, constructed from MRI data, and realistic box models of handset antennas [3]–[7].

The most complex head model that has been used so far by analytical techniques is the layered concentric spheres model [8] which comprises five spherical layers (skin, fat, bone, dura, CSF) and a brain tissue core. An extended Mie solution to the EM field induced in this head model was first obtained for plane-wave excitation [8] and [9]. Exposure to a linear dipole antenna or a loop antenna has been considered [10], albeit for an unrealistic exposure geometry and only for a specific frequency.

This paper serves two objectives. We introduce the layered eccentric spheres model for the head and we present an analytical solution to the induced EM field for time-harmonic localized source excitation; the simple case of plane-wave excitation is also treated.

The cardinal feature of the layered eccentric spheres model is the eccentricity between the inner and outer sets of concentric spherical layers which simulate brain and skull, respectively. The complex geometry of this model ensures better fitting to the head anatomy [11] than the concentric spheres model. Still, the eccentric spheres model is simple enough to permit an exact analytical solution to the wave equation, which we present in this paper. Eccentric spheres models have been used before within the framework of EEG and MEG research [11] and [12], which requires an analytical solution to the Laplace equation.

A compact IMM [13] analytical formulation is presented in Section II. We use multipolar expansions for the electric-field intensity in each region of the stratified structure and we apply the continuity of the fields across the spherical interfaces through surface integrals related to Green's vector theorem of the second kind. The end-result is a set of coupled linear equations for the wave amplitudes of the electric-field intensity, which can be solved by matrix-inversion. This analytical solution is actually an extended Mie solution for the eccentric spheres model.

Expressions for the wave amplitudes of the incident electric-field intensity are given in Section III for plane-wave excitation as well as for excitation from a general localized source. Application is made to a linear dipole antenna that carries sinusoidal current and to a small loop antenna that carries constant current.

Manuscript received October 10, 1995; revised May 17, 1996.

The authors are with the Department of Electrical and Computer Engineering, Aristotle University of Thessaloniki, Faculty of Technology, Division of Telecommunications, GR-54006 Thessaloniki, Greece, (3031) 996334.

Publisher Item Identifier S 0018-9480(96)07040-8.

Dielectric properties are assigned to the various layers of the head model through the Cole–Cole equation [14] which we fit to existing experimental data in Section IV. The numerical application of Section V is first focused on the total absorbed power in the head. We look into the effects of excitation frequency, exposure configuration, eccentricity, and antenna-head separation. We next investigate the internal deposition of EM energy in the head under linear dipole antenna exposure; we present plots of the absorption in each layer against the frequency and maps of the SAR distribution at specific cross sections of the head. The half-wavelength antenna is located at the side of the head and the excitation frequency is either 0.9 GHz or 1.9 GHz; these frequencies are typical for GSM (Group Speciale Mobile) or DECT (Digital European Cordless Telephone) phones, respectively.

II. Analytical Formulation

We consider a layered sphere with an eccentric layered spherical inclusion [Fig. 1(a)]. The center of the layered sphere O_1 will serve as origin of coordinates for the exterior (i.e., region 0) and the outer layers, whereas the center of the layered inclusion O_2 will be the origin of coordinates for the eccentric shell (i.e., region N_1), the inner layers and the spherical core (i.e., region N). With regard to the spherical coordinate system $(O_1; r_1\theta_1\phi_1)$ [Fig. 1(b)], O_2 is at $r_1 = d \leq \alpha_{N_1} - \alpha_{N_1+1}$, $\theta_1 = 0$. Each region of space is characterized by the wavenumber $k_i = \omega\sqrt{\mu_0\varepsilon_i}$, or, equivalently, by the (complex) refractive index $n_i = k_i/k_0$, the index i being $0, 1, 2, \cdots, N$. Free space is assumed for the exterior and harmonic time dependence $e^{-j\omega t}$ is implied throughout the analysis.

The electric field intensity in regions $i = 0, 1, \cdots, N$ is written as a sum of spherical multipoles

$$\vec{E}^i(\vec{r}) = \sum_{n=1}^{\infty} \sum_{m=-n}^{n} \mathcal{C}^i_{mn} \mathcal{W}^T_{mn}(k_i, \vec{r}) \tag{1}$$

where $\vec{r} = \vec{r}_1$, if $0 \leq i < N_1$, and $\vec{r} = \vec{r}_2$, if $N_1 \leq i \leq N$ [Fig. 1(b)]. $\mathcal{C}^i_{mn}$ represents a quadruplet of wave amplitudes

$$\mathcal{C}^i_{mn} = [a^i_{mn} \quad b^i_{mn} \quad c^i_{mn} \quad d^i_{mn}] \tag{2}$$

which will be determined through the analysis, whereas $\mathcal{W}_{mn}$ represents a quadruplet of vector spherical harmonics

$$\mathcal{W}_{mn}(k, \vec{r}) = [\vec{M}^{(1)}_{mn}(k, \vec{r}) \quad \vec{M}^{(3)}_{mn}(k, \vec{r}) \quad \vec{N}^{(1)}_{mn}(k, \vec{r}) \quad \vec{N}^{(3)}_{mn}(k, \vec{r})] \tag{3}$$

which constitute a complete set of solutions to the vector Helmholtz equation with respect to a spherical coordinate system [15]. The symbol T in the right-hand side of (1) is the transpose operator. The superscript (1) or (3) in the notation of vector spherical harmonics implies the use of the spherical Bessel function $j_n(kr)$ or of the spherical Hankel function $h^{(1)}_n(kr)$, respectively [16].

The wave amplitudes a^0_{mn}, c^0_{mn} and the vector spherical harmonics $\vec{M}^{(1)}_{mn}(k_0, \vec{r}_1)$, $\vec{N}^{(1)}_{mn}(k_0, \vec{r}_1)$ are used in the multipolar expansion of the incident electric field intensity $\vec{E}_{inc}(\vec{r}_1)$, which is part of $\vec{E}^0(\vec{r}_1)$; expressions for a^0_{mn}, c^0_{mn} are given in Section III for plane-wave excitation as well as for localized source excitation with $r_1 \leq R$. The scattered electric field intensity $\vec{E}_{sca}(\vec{r}_1) = \vec{E}^0(\vec{r}_1) - \vec{E}_{inc}(\vec{r}_1)$ is expressed through the wave amplitudes b^0_{mn}, d^0_{mn} and the

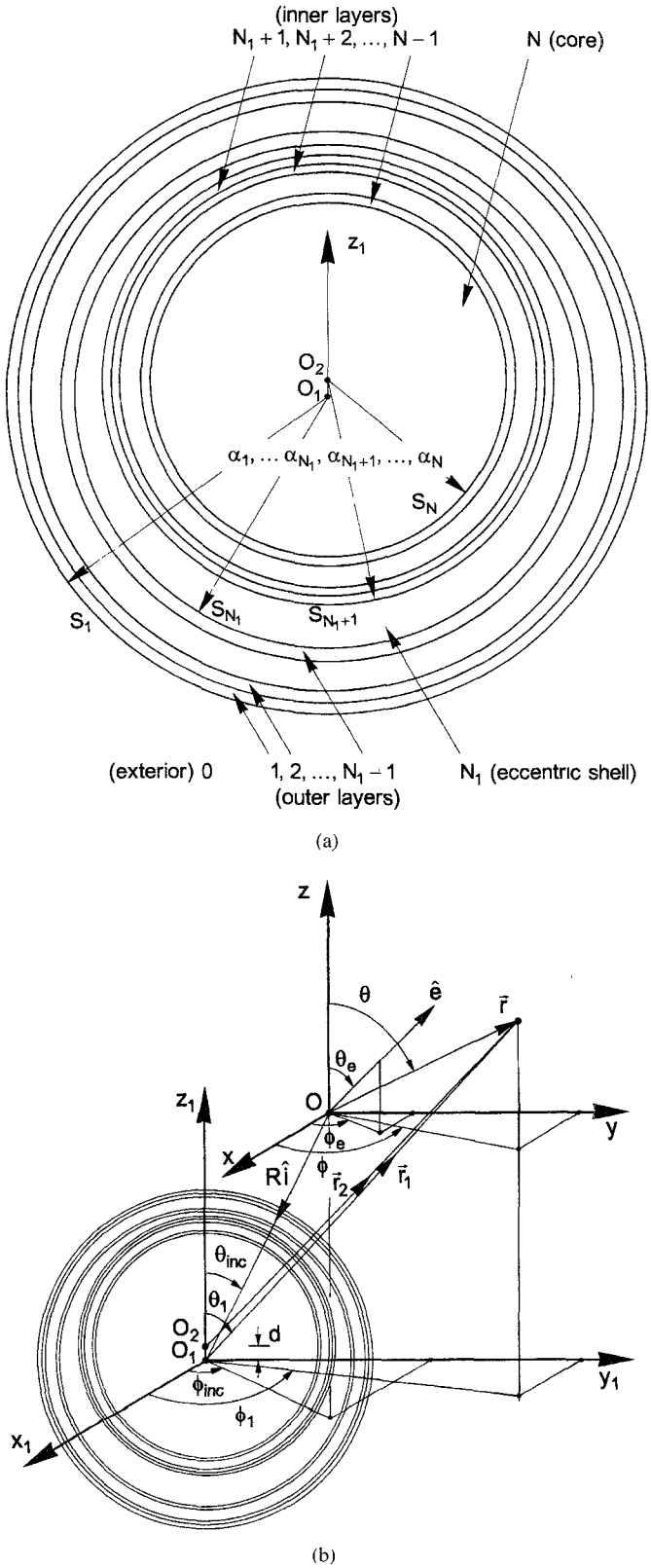

Fig. 1. (a) Cross section of layered eccentric spheres model and (b) excitation geometry.

vector spherical harmonics $\vec{M}_{mn}^{(3)}(k_0, \vec{r}_1)$, $\vec{N}_{mn}^{(3)}(k_0, \vec{r}_1)$. The latter involve the radial function $h_n^{(1)}(k_0 r_1)$, which, if $k_0 r_1 \gg 1$, represents an outgoing spherical wave with virtual origin at O_1 [16]. $\vec{E}^0(\vec{r}_1)$ is, therefore, regular at infinity. Moreover, since $\vec{E}^N(\vec{r}_2)$ must be regular at O_2, we set $b_{mn}^N = d_{mn}^N = 0$, thus avoiding the use of $h_n^{(1)}(k_N r_2)$ in the core.

An IMM equation of the first kind [13]

$$\oint_{S_{N_1}} [\vec{E}^{N_1-1} \times \nabla \times \vec{Q}^{N_1} - \vec{Q}^{N_1} \times \nabla \times \vec{E}^{N_1-1}] \cdot \hat{r}_1 \, ds = \oint_{S_{N_1+1}} [\vec{E}^{N_1+1} \times \nabla \times \vec{Q}^{N_1} - \vec{Q}^{N_1} \times \nabla \times \vec{E}^{N_1+1}] \cdot \hat{r}_2 \, ds \tag{4}$$

may be obtained from Green's vector theorem of the second kind, as applied to the eccentric shell for $\vec{E}^{N_1}(\vec{r}_2)$ and $\vec{Q}^{N_1}$; the latter may be any element of $\mathcal{W}_{kl}(k_{N_1}, \vec{r}_2)$ with $l = 1, 2, \cdots$ and $k = -l, \cdots, -1, 0, 1, \cdots, l$. If $\vec{Q}^{N_1} = \vec{M}_{kl}^{(1)}(k_{N_1}, \vec{r}_2)$ or $\vec{Q}^{N_1} = \vec{N}_{kl}^{(1)}(k_{N_1}, \vec{r}_2)$, (4) yields the following set of linear equations

$$\begin{aligned}
&\sum_{\nu=k'}^{\infty} [a_{-k\nu}^{N_1-1} U_\nu^{1\iota}(k_{N_1-1}, k_{N_1}, \alpha_{N_1}) A_{k\nu,1}^{kl} \\
&\quad + c_{-k\nu}^{N_1-1} V_\nu^{1\iota}(k_{N_1-1}, k_{N_1}, \alpha_{N_1}) B_{k\nu,1}^{kl} \\
&\quad + b_{-k\nu}^{N_1-1} U_\nu^{3\iota}(k_{N_1-1}, k_{N_1}, \alpha_{N_1}) A_{k\nu,1}^{kl} \\
&\quad + d_{-k\nu}^{N_1-1} V_\nu^{3\iota}(k_{N_1-1}, k_{N_1}, \alpha_{N_1}) B_{k\nu,1}^{kl}] \\
&\qquad = \left(\frac{\alpha_{N_1+1}}{\alpha_{N_1}}\right)^2 [a_{-kl}^{N_1+1} U_l^{1\iota}(k_{N_1+1}, k_{N_1}, \alpha_{N_1+1}) \\
&\quad + b_{-kl}^{N_1+1} U_l^{3\iota}(k_{N_1+1}, k_{N_1}, \alpha_{N_1+1})] \qquad (5a)
\end{aligned}$$

$$\begin{aligned}
&\sum_{\nu=k'}^{\infty} [a_{-k\nu}^{N_1-1} U_\nu^{1\iota}(k_{N_1-1}, k_{N_1}, \alpha_{N_1}) B_{k\nu,1}^{kl} \\
&\quad + c_{-k\nu}^{N_1-1} V_\nu^{1\iota}(k_{N_1-1}, k_{N_1}, \alpha_{N_1}) A_{k\nu,1}^{kl} \\
&\quad + b_{-k\nu}^{N_1-1} U_\nu^{3\iota}(k_{N_1-1}, k_{N_1}, \alpha_{N_1}) B_{k\nu,1}^{kl} \\
&\quad + d_{-k\nu}^{N_1-1} V_\nu^{3\iota}(k_{N_1-1}, k_{N_1}, \alpha_{N_1}) A_{k\nu,1}^{kl}] \\
&\qquad = \left(\frac{\alpha_{N_1+1}}{\alpha_{N_1}}\right)^2 [c_{-kl}^{N_1+1} V_l^{1\iota}(k_{N_1+1}, k_{N_1}, \alpha_{N_1+1}) \\
&\quad + d_{-kl}^{N_1+1} V_l^{3\iota}(k_{N_1+1}, k_{N_1}, \alpha_{N_1+1})] \qquad (5b)
\end{aligned}$$

where $k' = \max\{1, |k|\}$ and $\iota = 1$. If $\vec{Q}^{N_1} = \vec{M}_{kl}^{(3)}(k_{N_1}, \vec{r}_2)$ or $\vec{Q}^{N_1} = \vec{N}_{kl}^{(3)}(k_{N_1}, \vec{r}_2)$, (4) yields (5) with $\iota = 3$. The coupling coefficients $A_{k\nu,1}^{kl}$, $B_{k\nu,1}^{kl}$ originate from the translational addition theorem for vector spherical harmonics, as applied to the translation from O_2 to O_1 (see Appendix A). Details about the evaluation of the surface integrals in (4) may be found in Appendix B of [13]. The abbreviations

$$\begin{aligned}
&U_n^{\iota_1\iota_2}(u, v, r) \\
&\quad = \frac{2n(n+1)}{2n+1} \\
&\qquad \cdot [v z_n^{(\iota_1)}(ur) \eta_n^{(\iota_2)}(vr) - u \eta_n^{(\iota_1)}(ur) z_n^{(\iota_2)}(vr)] \qquad (6a) \\
&V_n^{\iota_1\iota_2}(u, v, r) \\
&\quad = \frac{2n(n+1)}{2n+1} \\
&\qquad \cdot [u z_n^{(\iota_1)}(ur) \eta_n^{(\iota_2)}(vr) - v \eta_n^{(\iota_1)}(ur) z_n^{(\iota_2)}(vr)] \qquad (6b)
\end{aligned}$$

have been used in (5); $z_n^{(\iota)}(kr)$ represents $j_n(kr)$ or $h_n^{(1)}(kr)$ for $\iota = 1$ or $\iota = 3$, respectively, and $\eta_n^{(\iota)}(kr) = [krz_n^{(\iota)}(kr)]'/kr$, the prime implying differentiation with respect to kr. The superscripts ι_1, ι_2 in (6) stand for 1 or 3.

The continuity of the fields across the spherical interface S_i between any two regions $i-1$ and i [Fig. 1(a)] is enforced through an IMM equation of the second kind [13]

$$\oint_{S_i} [\vec{E}^{i-1} \times \nabla \times \vec{Q} - \vec{Q} \times \nabla \times \vec{E}^{i-1}] \cdot \hat{r} \, ds = \oint_{S_i} [\vec{E}^{i} \times \nabla \times \vec{Q} - \vec{Q} \times \nabla \times \vec{E}^{i}] \cdot \hat{r} \, ds \tag{7}$$

where $\vec{Q}$ is any element of $\mathcal{W}_{kl}(k_{i-1}, \vec{r})$ or $\mathcal{W}_{kl}(k_i, \vec{r})$. Equation (7) is simply a synoptic expression of the continuity of the tangential components of the electric- and magnetic-field intensities throughout S_i.

On the one hand, by use of $\vec{M}_{kl}^{(1)}(k_{i-1}, \vec{r})$, $\vec{M}_{kl}^{(3)}(k_{i-1}, \vec{r})$, $\vec{N}_{kl}^{(1)}(k_{i-1}, \vec{r})$ or $\vec{N}_{kl}^{(3)}(k_{i-1}, \vec{r})$ as $\vec{Q}$, (7) yields the matrix equation

$$\mathcal{C}_{mn}^{i-1} = \mathcal{C}_{mn}^{i} \mathcal{T}_n^{i-1,i} \tag{8}$$

where $\mathcal{T}_n^{i-1,i}$ is the 4×4 transfer matrix for the inward crossing of S_i. On the other hand, by use of $\vec{M}_{kl}^{(1)}(k_i, \vec{r})$, $\vec{M}_{kl}^{(3)}(k_i, \vec{r})$, $\vec{N}_{kl}^{(1)}(k_i, \vec{r})$ or $\vec{N}_{kl}^{(3)}(k_i, \vec{r})$ as $\vec{Q}$, (7) yields the matrix equation

$$\mathcal{C}_{mn}^{i} = \mathcal{C}_{mn}^{i-1} \mathcal{T}_n^{i,i-1} \tag{9}$$

where $\mathcal{T}_n^{i,i-1}$ is the 4×4 transfer matrix for the outward crossing of S_i. Both $\mathcal{T}_n^{i-1,i}$ and $\mathcal{T}_n^{i,i-1}$ are obtained from the definition given in (10) as shown at the bottom of the page where $|\iota' - \iota| = 1$. The abbreviations

$$I_n^{\iota_1\iota_2\iota_3}(u, v, r) = \frac{U_n^{\iota_1\iota_3}(u, v, r)}{U_n^{\iota_2\iota_3}(v, v, r)} \tag{11a}$$

$$J_n^{\iota_1\iota_2\iota_3}(u, v, r) = \frac{V_n^{\iota_1\iota_3}(u, v, r)}{V_n^{\iota_2\iota_3}(v, v, r)} \tag{11b}$$

have been used in (10) with ι_1, ι_2, ι_3 equal to 1 or 3.

$$\mathcal{T}_n^{\iota,\iota'} = \begin{bmatrix} I_n^{113}(k_{\iota'}, k_\iota, \alpha_\iota) & I_n^{131}(k_{\iota'}, k_\iota, \alpha_\iota) & 0 & 0 \\ I_n^{313}(k_{\iota'}, k_\iota, \alpha_\iota) & I_n^{331}(k_{\iota'}, k_\iota, \alpha_\iota) & 0 & 0 \\ 0 & 0 & J_n^{113}(k_{\iota'}, k_\iota, \alpha_\iota) & J_n^{131}(k_{\iota'}, k_\iota, \alpha_\iota) \\ 0 & 0 & J_n^{313}(k_{\iota'}, k_\iota, \alpha_\iota) & J_n^{331}(k_{\iota'}, k_\iota, \alpha_\iota) \end{bmatrix} \tag{10}$$

By iterative application of (8), we obtain the matrix equation

$$\mathcal{C}_{mn}^{N_1+1} = \mathcal{C}_{mn}^{N}\mathcal{T}_n^{in} \tag{12}$$

where $\mathcal{T}_n^{in} = T_n^{N-1,N}T_n^{N-2,N-1}\cdots T_n^{N_1+1,N_1+2}$ is the transfer matrix associated with the inward crossing through the inner layers. Moreover, by iterative application of (9) we obtain the matrix equation

$$\mathcal{C}_{mn}^{N_1-1} = \mathcal{C}_{mn}^{0}\mathcal{T}_n^{out} \tag{13}$$

where $\mathcal{T}_n^{out} = T_n^{1,0}T_n^{2,1}\cdots T_n^{N_1-1,N_1-2}$ is the transfer matrix associated with the outward crossing through the outer layers. By use of (12) and (13), we introduce a_{mn}^{N}, c_{mn}^{N} and b_{mn}^{0}, d_{mn}^{0} in (5) and, by elimination of a_{mn}^{N}, c_{mn}^{N}, we finally obtain a pair of coupled linear equations for the wave amplitudes b_{mn}^{0}, d_{mn}^{0} of $\vec{E}_{sca}(\vec{r}_1)$

$$\sum_{\nu=k'}^{\infty}\mathcal{C}_{-k\nu}^{0}\mathcal{T}_{\nu}^{out}\mathcal{O}_1^{T} = 0 \tag{14a}$$

$$\sum_{\nu=k'}^{\infty}\mathcal{C}_{-k\nu}^{0}\mathcal{T}_{\nu}^{out}\mathcal{O}_2^{T} = 0 \tag{14b}$$

$\mathcal{O}_1$ and $\mathcal{O}_2$ are 1×4 matrices

$$\mathcal{O}_1 = [\Omega_k^{(1)}(U_\nu, Y_l)\ \ \Omega_k^{(3)}(U_\nu, Y_l)\ \ \Omega_k^{(1)}(V_\nu, Y_l)\ \ \Omega_k^{(3)}(V_\nu, Y_l)] \tag{15a}$$

$$\mathcal{O}_2 = [\Omega_k^{(1)}(U_\nu, Z_l)\ \ \Omega_k^{(3)}(U_\nu, Z_l)\ \ \Omega_k^{(1)}(V_\nu, Z_l)\ \ \Omega_k^{(3)}(V_\nu, Z_l)] \tag{15b}$$

with elements given by the definition

$$\begin{aligned}\Omega_k^{(\iota)}(\mathrm{X}_\nu, \Psi_l) &= F_{k\nu,1}^{kl}[X_\nu^{\iota 1}(k_{N_1-1}, k_{N_1}, \alpha_{N_1})\Psi_l^3(k_{N_1+1}, k_{N_1}, \alpha_{N_1+1}) \\ &\quad - X_\nu^{\iota 3}(k_{N_1-1}, k_{N_1}, \alpha_{N_1})\Psi_l^1(k_{N_1+1}, k_{N_1}, \alpha_{N_1+1})]\end{aligned} \tag{16}$$

where $X_\nu^{\iota_1\iota_2}$ stands for $U_\nu^{\iota_1\iota_2}$ or $V_\nu^{\iota_1\iota_2}$ and Ψ_l^{ι} stands for Y_l^{ι} or Z_l^{ι}. The latter are defined as follows

$$\begin{aligned}Y_n^{\iota}(u, v, r) &= U_n^{1\iota}(u, v, r)\mathcal{T}_n^{in}(1, 1) \\ &\quad + U_n^{3\iota}(u, v, r)\mathcal{T}_n^{in}(1, 2)\end{aligned} \tag{17a}$$

$$\begin{aligned}Z_n^{\iota}(u, v, r) &= V_n^{1\iota}(u, v, r)\mathcal{T}_n^{in}(3, 3) \\ &\quad + V_n^{3\iota}(u, v, r)\mathcal{T}_n^{in}(3, 4)\end{aligned} \tag{17b}$$

where $\mathcal{T}_n^{in}(i, j)$ is the element of $\mathcal{T}_n^{in}$ in the ith row and the jth column. Finally, $F_{k\nu,1}^{kl}$ in (16) stands for $A_{k\nu,1}^{kl}$ or $B_{k\nu,1}^{kl}$ according to the scheme

$$F_{k\nu,1}^{kl} = \begin{cases} A_{k\nu,1}^{kl} \\ B_{k\nu,1}^{kl}\end{cases}$$

if

$$(X_\nu, \Psi_l) = \begin{cases} (U_\nu, Y_l) & \text{or} \quad (V_\nu, Z_l) \\ (U_\nu, Z_l) & \text{or} \quad (V_\nu, Y_l)\end{cases}. \tag{18}$$

In order to solve for b_{mn}^{0}, d_{mn}^{0} we truncate the infinite summations in the left hand side of (14). Let M be the appropriate truncation number; the choice of M is discussed in Section V. Since $\max\{1, |k|\} = k' \le \nu \le M$, there are $2(M-k'+1)$ unknowns in (14), but only two equations for them. However, the subscript l of the testing wavefunctions $\vec{M}_{kl}^{(1)}(k_{N_1}, \vec{r}_2)$, $\vec{M}_{kl}^{(3)}(k_{N_1}, \vec{r}_2)$, $\vec{N}_{kl}^{(1)}(k_{N_1}, \vec{r}_2)$, and $\vec{N}_{kl}^{(3)}(k_{N_1}, \vec{r}_2)$, used in (4), can also be varied in the range $[k', M]$. Thus $2(M-k'+1)$ equations are obtained for the $2(M-k'+1)$ unknowns. That set yields b_{mn}^{0}, d_{mn}^{0} with $m = -k$ and $k' \le n \le M$. The wave amplitudes b_{mn}^{0}, d_{mn}^{0} with $-M \le m \le M$ and $\max\{1, |m|\} \le n \le M$ can be determined by varying k from $-M$ to M and repeating the above steps.

Once b_{mn}^{0}, d_{mn}^{0} have been determined, the wave amplitudes in the outer layers can be determined through the matrix equation $\mathcal{C}_{mn}^{\imath} = \mathcal{C}_{mn}^{0}\mathcal{T}_n^{1,0}\mathcal{T}_n^{2,1}\cdots\mathcal{T}_n^{\imath,\imath-1}$ with $\imath = 1, 2, \cdots, N_1-1$. Knowing $a_{mn}^{N_1-1}$, $b_{mn}^{N_1-1}$, $c_{mn}^{N_1-1}$, $d_{mn}^{N_1-1}$, we obtain $a_{mn}^{N_1+1}$, $b_{mn}^{N_1+1}$, $c_{mn}^{N_1+1}$, $d_{mn}^{N_1+1}$ from (5) and subsequently a_{mn}^{N}, c_{mn}^{N} from (12). The wave amplitudes in the inner layers can be obtained from the matrix equation $\mathcal{C}_{mn}^{\imath} = \mathcal{C}_{mn}^{N}\mathcal{T}_n^{N-1,N}\mathcal{T}_n^{N-2,N-1}\cdots\mathcal{T}_n^{\imath,\imath+1}$ with $i = N_1, N_1+1, \cdots, N-1$. This completes the exact IMM solution for the wave amplitudes of the electric field intensity throughout the layered structure. The wave amplitudes a_{mn}^{0}, c_{mn}^{0} of $\vec{E}_{inc}(\vec{r}_1)$, which were so far assumed to be known, are determined next.

III. Excitation

The simplest excitation is provided by a linearly polarized plane EM wave. Without loss of generality we may assume that the incidence direction $\hat{i}$ is in the coordinate plane $x_1O_1z_1$ [Fig. 1(b)]. Hence, $\phi_{inc} = 0$ and the incident wavenumber vector is $\vec{k}_{inc} = k_0\hat{i} = -\omega\sqrt{\mu_0\varepsilon_0}(\hat{x}_1\sin\theta_{inc} + \hat{z}_1\cos\theta_{inc})$. The wave amplitudes a_{mn}^{0}, c_{mn}^{0} of the multipolar expansion for $\vec{E}_{inc}(\vec{r}_1)$ are given by [13]

$$\begin{aligned}a_{mn}^{0} &= (-1)^m j^n\frac{2n+1}{\sqrt{n(n+1)}}\hat{e} \\ &\quad\cdot\vec{C}_{-mn}(\theta = \pi-\theta_{inc}, \phi = \pi)\end{aligned} \tag{19a}$$

$$\begin{aligned}c_{mn}^{0} &= (-1)^{m+1} j^{n+1}\frac{2n+1}{\sqrt{n(n+1)}}\hat{e} \\ &\quad\cdot\vec{B}_{-mn}(\theta = \pi-\theta_{inc}, \phi = \pi)\end{aligned} \tag{19b}$$

where $\vec{B}_{mn}(\theta, \phi)$, $\vec{C}_{mn}(\theta, \phi)$ are complex spherical surface vector functions [15] and $\hat{e}$ is the polarization vector.

More realistic excitation of the layered structure is provided by a nearby localized source which is enclosed in a spherical region V centered at O [Fig. 1(b)]. This localized source is represented by a current density $\vec{J}(\vec{r})$ and a charge density $\rho(\vec{r}) = \nabla\cdot\vec{J}(\vec{r})/j\omega$, both expressed with respect to the local spherical coordinate system $(O; r\theta\phi)$. The wave amplitudes a_{mn}^{0}, c_{mn}^{0} of the multipolar expansion for $\vec{E}_{inc}(\vec{r}_1)$ are given by

$$a_{mn}^{0} = \sum_{\nu=1}^{\infty}\sum_{\mu=-\nu}^{\nu}[b_{\mu\nu}^{inc}A_{mn,3}^{\mu\nu} + d_{\mu\nu}^{inc}B_{mn,3}^{\mu\nu}] \tag{20a}$$

$$c_{mn}^{0} = \sum_{\nu=1}^{\infty}\sum_{\mu=-\nu}^{\nu}[b_{\mu\nu}^{inc}B_{mn,3}^{\mu\nu} + d_{\mu\nu}^{inc}A_{mn,3}^{\mu\nu}] \tag{20b}$$

where

$$b_{\mu\nu}^{inc} = Z_0 \frac{k_0^2}{4\pi} \frac{2\nu+1}{\nu(\nu+1)} \frac{(\nu-\mu)!}{(\nu+\mu)!} \int_V \nabla \cdot (\vec{r}\times\vec{J}) j_\nu(k_0 r) P_\nu^\mu(\cos\theta) e^{-j\mu\phi}\, dv \quad (21a)$$

$$d_{\mu\nu}^{inc} = j \frac{k_0^2}{4\pi} \frac{2\nu+1}{\nu(\nu+1)} \frac{(\nu-\mu)!}{(\nu+\mu)!} \int_V \cdot \left[\frac{\rho}{\varepsilon_0} \eta_\nu^{(1)}(k_0 r) + j\omega\mu_0(\vec{r}\cdot\vec{J}) j_\nu(k_0 r)\right] \cdot P_\nu^\mu(\cos\theta) e^{-j\mu\phi}\, dv \quad (21b)$$

are the wave amplitudes of the multipolar expansion for $\vec{E}_{inc}(\vec{r} = R\hat{i} + \vec{r}_1)$ [17]. $A_{mn,3}^{\mu\nu}$, $B_{mn,3}^{\mu\nu}$ are the coupling coefficients associated with the translation of vector spherical harmonics from O to O_1 (see Appendix A), $Z_0 = \sqrt{\mu_0/\varepsilon_0}$ is the intrinsic impedance of free space and $P_\nu^\mu(\cos\theta)$ is an associated Legendre function of the first kind [18]. The expressions of (20) and (21) are valid for $r_1 \le R$, where R is the distance of O_1 from O, and outside the source region V.

We first consider a linear dipole antenna of length l, centered at O, and directed along the arbitrary polarization vector $\hat{e}$ [Fig. 1(b)]. This localized source is represented by a spherical source region V of radius $l/2$, wherein the current density is $\vec{J}(\vec{r}) = I(r)\hat{r}[\delta(\theta-\theta_e)\delta(\phi-\phi_e) - \delta(\theta-\pi+\theta_e)\delta(\phi-\pi-\phi_e)]$; the corresponding charge density $\rho(\vec{r})$ can be obtained from the equation of continuity. The wave amplitudes a_{mn}^0, c_{mn}^0 of (20) can be used for $\vec{E}_{inc}(\vec{r}_1)$, provided that $r_1 \le R - l/2$. If $I(r) = I_0 \sin[k_0(l-2r)/2]$, (21) yields $b_{\mu\nu}^{inc} = 0$ and

$$d_{\mu\nu}^{inc} = -30k_0^2(I_0 l)[1-\cos(\nu\pi)] \frac{2\nu+1}{2\nu(\nu+1)} \frac{(\nu-\mu)!}{(\nu+\mu)!} \cdot j_\nu\left(\frac{k_0 l}{2}\right) P_\nu^\mu(\cos\theta_e) e^{-j\mu\phi_e} \quad (22)$$

If $\hat{e} = \hat{z}$, (22) is simplified as follows:

$$d_{\mu\nu}^{inc} = -30k_0^2(I_0 l)\delta_{\mu,0}[1-\cos(\nu\pi)] \cdot \frac{2\nu+1}{2\nu(\nu+1)} j_\nu\left(\frac{k_0 l}{2}\right) \quad (23)$$

where $\delta_{\mu,0}$ is a Kronecker delta; (23) indicates that $d_{\mu\nu}^{inc} = 0$ unless $\mu = 0$ and ν is odd.

We also consider a $\hat{z}$-oriented magnetic dipole at O, which is a circular current loop centered at O; the plane of the loop is normal to $\hat{z}$. Let α_0 be the radius of the loop, which is assumed to carry constant current I_0. This localized source is represented by a spherical source region V of radius α_0, wherein the current density is $\vec{J}(\vec{r}) = (I_0/\alpha_0)\hat{\phi}\delta(\theta - \pi/2)\delta(r-\alpha_0)$; the corresponding charge density is zero. Equation (21) now yields $d_{\mu\nu}^{inc} = 0$ and

$$b_{\mu\nu}^{inc} = Z_0 k_0^2(I_0\alpha_0)\delta_{\mu,0}[1-\cos(\nu\pi)] \cdot \frac{2\nu+1}{2\nu(\nu+1)} j_\nu(k_0\alpha_0)\left[\frac{dP_\nu}{d\theta}\right]_{\theta=\pi/2} \quad (24)$$

where $P_\nu(\cos\theta)$ is a Legendre polynomial [16]. The wave amplitudes a_{mn}^0, c_{mn}^0 of (20) can be used for $\vec{E}_{inc}(\vec{r}_1)$ if $r_1 \le R - \alpha_0$.

TABLE I
SIX-LAYER MODEL OF HUMAN HEAD

Layer	Density*	Radius**	ε_∞	ε_s	σ_s	f_c [Hz]	α
Skin	1.10	9	23.1	17.698	0.309	46.5	0.578
Fat	1.85	8.9	2.63×10^{-5}	14.93	0.242	8.25×10^9	0.194
Bone	1.85	8.76	2.63×10^{-5}	14.93	0.242	8.25×10^9	0.194
Dura	1.10	8.35	23.1	17.968	0.309	46.5	0.578
CSF	1.06	8.3	5	74	2	25	0
Brain	1.03	8.1	27.85	15.777	0.416	5.92	0.651

* [10^3 **kg/m^3**]
** **[cm]**

IV. HEAD MODEL

The theory is applied to a six-layer eccentric spheres model of the human head. The outer set of layers comprises skin and fat tissue layers enclosing an eccentric bone shell. The inner set of layers comprises dura and CSF tissue layers enclosing a brain core. The model allows for eccentricity between the outer and the inner layers. Eccentricity may range from $d = 0$ (i.e., concentric spheres model) to $d = \alpha_3 - \alpha_4$. The overall radius of the head is 9 cm. Values for the outer radius [8] and the density [3] of the various layers are given in Table I.

The dielectric properties of tissues depend on the cellular tissue structure and they are characterized by strong (α-, β-, and γ-dispersions) and weak (δ-dispersion) relaxation phenomena [14]. The frequency band of interest for our study (i.e., 0.1–3 GHz) is at the low end of the γ-dispersion which is due to the relaxation of free tissue water; the relaxation frequency is 25 GHz at 37°C. Moreover, there may be significant contribution from δ-dispersion [19] in this frequency band; δ-dispersion, being rather poorly defined, is mostly attributed to the relaxation of water bound to protein molecules. In order to account for several relaxation mechanisms, we represent the dielectric properties of tissues by the Cole–Cole equation

$$\varepsilon^* = \varepsilon_\infty + \frac{\varepsilon_s - \varepsilon_\infty}{1 + \left(\frac{-jf}{f_c}\right)^{1-\alpha}} + j\frac{\sigma_s}{2\pi f \varepsilon_0} \quad (25)$$

which is a well-known empirical approximation [14] for the dielectric properties of systems that exhibit a wide variety of effective relaxation times; ε^* in (25) is the complex permittivity, f is the frequency, and ε_0 is the permittivity of free space. The model parameters ε_∞, ε_s, σ_s, f_c, α are estimated by fitting (25) to experimental data from the literature [20]–[29]. Non-linear least squares estimates of the parameters are presented in Table I for all the tissues involved. As the frequency band of interest does not cover an entire dispersion range, the estimated parameters have only limited physical significance. Yet, they reproduce to within 10% the experimental data in the frequency range from 0.1–3 GHz.

Skin data of Grant *et al.* [20] and Tamura *et al.* [21] were used. Identical dielectric properties were considered for the fat and bone layers; the experimental data of [22] and [23] were used for fat and bone tissue. The dielectric properties of dura were assumed to be identical to those of skin. The dielectric properties of CSF, which is 99% water, were approximated by those of pure water [24] with the addition of a DC conductivity

$\sigma_s = 2$ S/m, which is typical for physiological saline solutions [25]. Because of the diversity of published data for brain tissue, average values from several references [22], [26]–[29] were used.

We currently investigate the sensitivity of calculated results to uncertainties of the dimensions and the dielectric properties of the layered eccentric spheres model of the head. Preliminary results suggest that the most critical parameters are the overall radius, the thickness of the fat-bone layer and the dielectric properties of the brain.

V. Numerical Results and Discussion

We checked this theoretical solution in several ways. Energy conservation was checked for plane-wave excitation by use of the following equation:

$$\frac{1}{2}\sum_{i=1}^{N}\int_{V_i}\sigma_i|\vec{E}^i|^2\,dv = \frac{1}{2Z_0}\left[\frac{4\pi}{k_0}\,\mathrm{Im}\{\vec{f}(\hat{i},\hat{i})\}\cdot\hat{e} - \int_0^{2\pi}\int_0^{\pi}|\vec{f}(\hat{i},\hat{r}_1)|^2\sin\theta_1\,d\theta_1\,d\phi_1\right] \quad (26)$$

σ_i stands for the conductivity of region i, which occupies volume V_i, and $\vec{f}(\hat{i},\hat{r}_1)$ is the scattering amplitude which is introduced through the far-field expression $\vec{E}_{sca}(\vec{r}_1) = \vec{f}(\hat{i},\hat{r}_1)e^{jk_0r_1}/r_1$; the latter is valid for $k_0r_1 \gg 1$. Each side of (26) represents the total absorbed power, the right-hand side resulting from the optical theorem [30]. Energy conservation is checked by independent calculations of each side of (26); the energy error of our solution was generally less than 0.1%. The principle of reciprocity was checked by use of the equation $|\vec{f}(\hat{i},\hat{r}_1)| = |\vec{f}(-\hat{r}_1,-\hat{i})|$. Reciprocity checks were equally successful. Although the above are only necessary conditions for the validity of any solution, it is reassuring that our solution successfully passed both tests.

More confidence in this solution was gained by comparisons with existing computational results [2], [8], and [9] for the concentric spheres model of the head, which is a special case of our model. We reproduced accurately Figs. 5 and 6 of [2] and Figs. 2 and 3 of [9]. Since we found no evidence against the veracity of this solution, we decided, for the sake of brevity, to omit numerical results concerning checks and comparisons.

The computational load associated with our solution depends mainly on the length of the truncated multipolar expansions and only slightly on the number of layers. Four-digit convergence was achieved for the head model of Section IV with truncation number $9 \le M \le 11$. Convergence is generally slower when the eccentricity is maximum (i.e., $d = \alpha_3 - \alpha_4$).

Our numerical application is first focused on the total absorbed power (i.e., the average SAR). The calculations were made as indicated by the left-hand side of (26). Plane-wave excitation is considered in Fig. 2(a). The direction of incidence is $\hat{i} = -\hat{z}_1$ or $\hat{i} = -\hat{x}_1$, the polarization vector $\hat{e}$ being parallel to the coordinate plane $x_1O_1z_1$ [Fig. 1(b)]. The eccentricity is $d = 0$ (curve 1), $d = 2$ mm (curves 2, 3), and $d = 4$ mm (curves 4, 5). The total absorbed power is normalized with respect to the power normally incident upon a circular area of

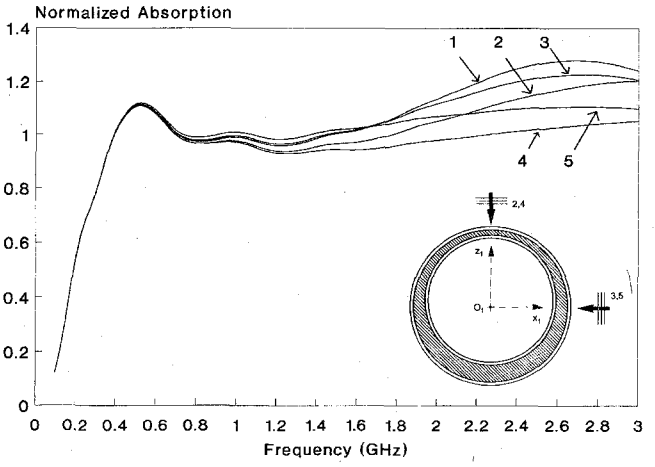

(a)

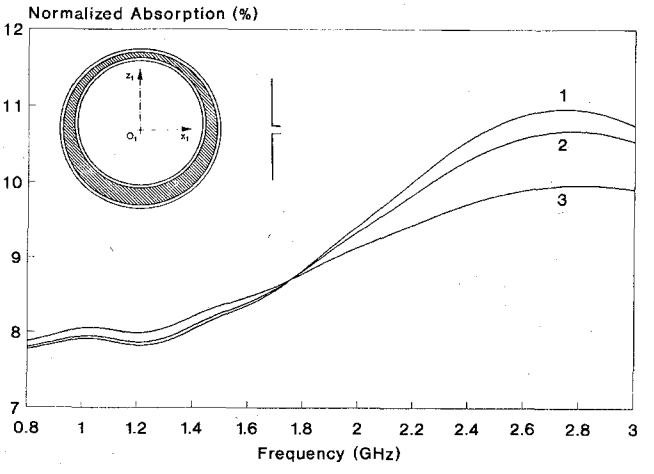

(b)

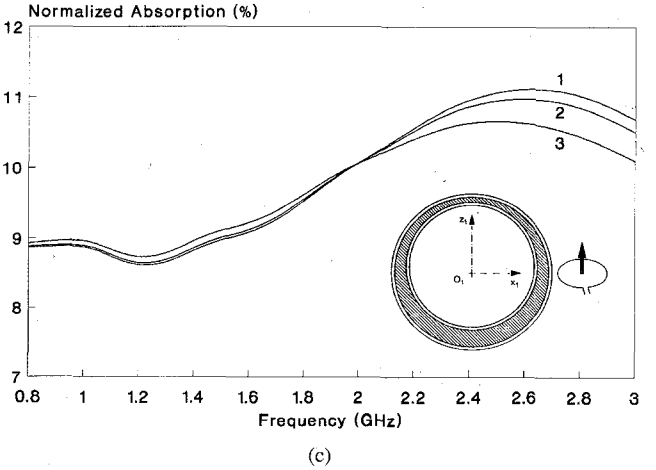

(c)

Fig. 2. Normalized total absorbed power P_a/P_{inc} versus frequency $f = \omega/2\pi$: (a) plane-wave excitation ($\hat{i} = -\hat{z}_1$, $\hat{e} = \hat{x}$ or $\hat{i} = -\hat{x}_1$, $\hat{e} = -\hat{z}$); eccentricity $d = 0$ 1) $d = 2$ mm 2), 3) $d = 4$ mm 4), 5); P_{inc} is the incident power intercepted by the geometric cross section, (b) Half-wavelength linear dipole antenna ($\phi_{inc} = 0°$, $\theta_{inc} = 90°$, $R = 19$ cm, $\hat{e} = \hat{z}$); eccentricity $d = 0$ 1) $d = 2$ mm 2) $d = 4$ mm 3); P_{inc} is the power radiated by the antenna, and (c) loop antenna ($\phi_{inc} = 0°$, $\theta_{inc} = 90°$, $R = 19$ cm, $\hat{e} = \hat{z}$, $k_0\alpha = 0.2$); eccentricity $d = 0$ 1) $d = 2$ mm 2) $d = 4$ mm 3); P_{inc} is the power radiated by the antenna.

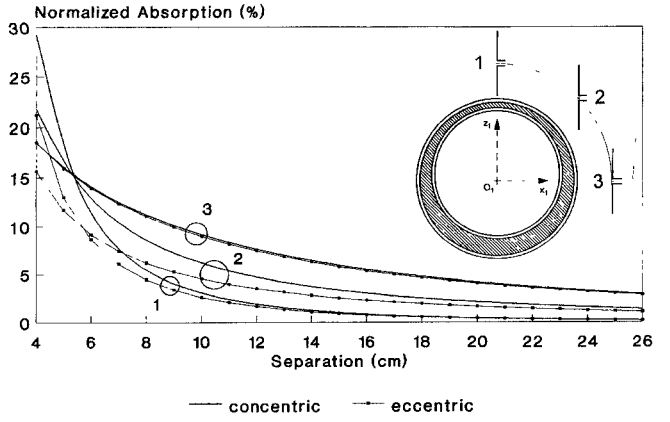

Fig. 3. Normalized total absorbed power P_a/P_{inc} versus separation $R-\alpha_1$ from linear dipole antenna; $f = 1.9$ GHz, $l = \lambda/2$, $\hat{e} = \hat{z}$, $\phi_{inc} = 0°$, $\theta_{inc} = 0°$ 1) $\theta_{inc} = 45°$ 2) $\theta_{inc} = 90°$ 3); eccentricity $d = 0$ or $d = 2$ mm; P_{inc} is the power radiated by the antenna.

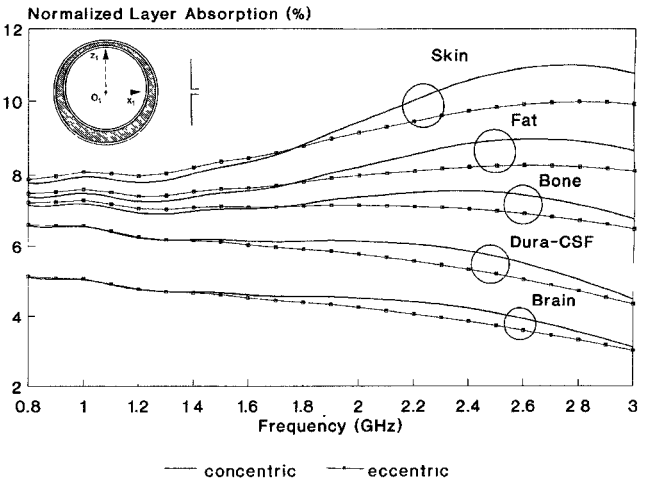

Fig. 4. Layer distribution of normalized absorbed power P_a/P_{inc}; linear dipole antenna $l = \lambda/2$, $\hat{e} = \hat{z}$, $\phi_{inc} = 0°$, $\theta_{inc} = 90°$, $R = 19$ cm; eccentricity $d = 0$ 1) or $d = 4$ mm 2); P_{inc} is the power radiated by the antenna.

radius α_1. Absorption is weak at low frequencies; the layered structure exhibits a resonance behavior as the frequency is increased. The first peak of the absorption characteristic occurs at 0.525 GHz; this peak is related to the overall size of the layered structure, as compared to the incident wavelength. Subsequent peaks are related to layer resonance [3]. The effect of eccentricity is more pronounced at high frequencies. Eccentricity may be responsible for up to 20% reduction of the total absorbed power from the level corresponding to the concentric spheres model. Endfire incidence (i.e., $\hat{i} = -\hat{z}_1$) is most sensitive to eccentricity.

Exposure to a linear dipole antenna [Fig. 2(b)] or a loop antenna [Fig. 2(c)] are discussed next. The antenna is at the side of the layered structure, the eccentricity is $d = 0$, 2 mm or 4 mm, the antenna-head separation is $R - \alpha_1 = 10$ cm, and the total absorbed power is given as percentage of the power radiated by the antenna. Strong absorption occurs above 2 GHz. As only broadside incidence (i.e., $\hat{i} = -\hat{x}_1$) is considered in Fig. 2(b) and (c), the reduction of absorption due to nonzero eccentricity is only up to 10% of the reference level. By comparison of Fig. 2(b) and (c), it is verified that absorption is slightly stronger for the loop antenna excitation.

The dependence of absorption on the separation $(R - \alpha_1)$ between the layered structure and the feed-point of a half-wavelength linear dipole antenna is displayed in Fig. 3. The antenna is in the coordinate plane $x_1O_1z_1$ and it is parallel to the z_1-axis. Thick curves correspond to the concentric spheres model, whereas those marked by small squares correspond to the eccentric spheres model.

The principal remark incited by Fig. 3 is that the total absorbed power, which is again given as percentage of the power radiated by the antenna, decreases as the separation is increased for all three antenna locations. If the separation is small, absorption is strongest with the antenna along the z_1-axis (i.e., $\theta_{inc} = 0°$); the antenna is then closest to the head. The opposite is true for large separations: absorption is strongest with the antenna at the side of the layered structure (i.e., $\theta_{inc} = 90°$), a reasonable outcome since the target is then in the direction of maximum radiation from the antenna. Eccentricity again manifests itself as a reduction of the total absorbed power from the value that corresponds to the concentric spheres model. The effect of eccentricity is more pronounced for small separations. It is remarkable that on endfire incidence (i.e., $\theta_{inc} = 0°$) a small value of the eccentricity ($d = 2$ mm) results in more than 25% reduction of the total absorbed power. On broadside incidence (i.e., $\theta_{inc} = 90°$) absorption is less sensitive to eccentricity for any separation.

Interest is next focused on the internal distribution of the absorbed power. Each curve of Fig. 4 displays the power absorbed in the volume enclosed by the outer surface of the indicated layer. Thick curves correspond to the concentric spheres model, whereas those marked by small squares correspond to the eccentric spheres model with $d = 4$ mm. The uppermost pair of curves display the frequency-dependence of the total absorbed power. Excitation by a half-wavelength linear dipole antenna at the side of the layered structure is considered; the antenna-head separation is $R - \alpha_1 = 10$ cm.

The lowermost pair of curves corresponds to absorption by the brain; more than half of the total absorption occurs in the brain at frequencies below 1.5 GHz. Substantial absorption occurs in the highly conductive CSF layer throughout this frequency band; absorption by dura is negligible. The contribution of the outer layers (i.e., bone, fat, and skin) is considerable at high frequencies, as a result of the decreased penetration depth; more than half of the total absorption occurs in the outer layers at 2.7 GHz. The effect of eccentricity is most pronounced at a specific frequency for each layer, which is higher for superficial layers.

Finally, we examine the SAR distribution in two cross sections of the layered structure. The excitation frequency is 0.9 GHz in Fig. 5 and the antenna-head separation is 8.5 cm. Fig. 5(a) displays the SAR distribution in the coordinate plane $x_1O_1y_1$, whereas Fig. 5(b) and (c) refer to the coordinate plane $x_1O_1z_1$. Fig. 5(a) and (b) correspond to the concentric spheres model; the cardinal remarks are that (a) absorption is mainly superficial and (b) most absorption occurs on the side nearest

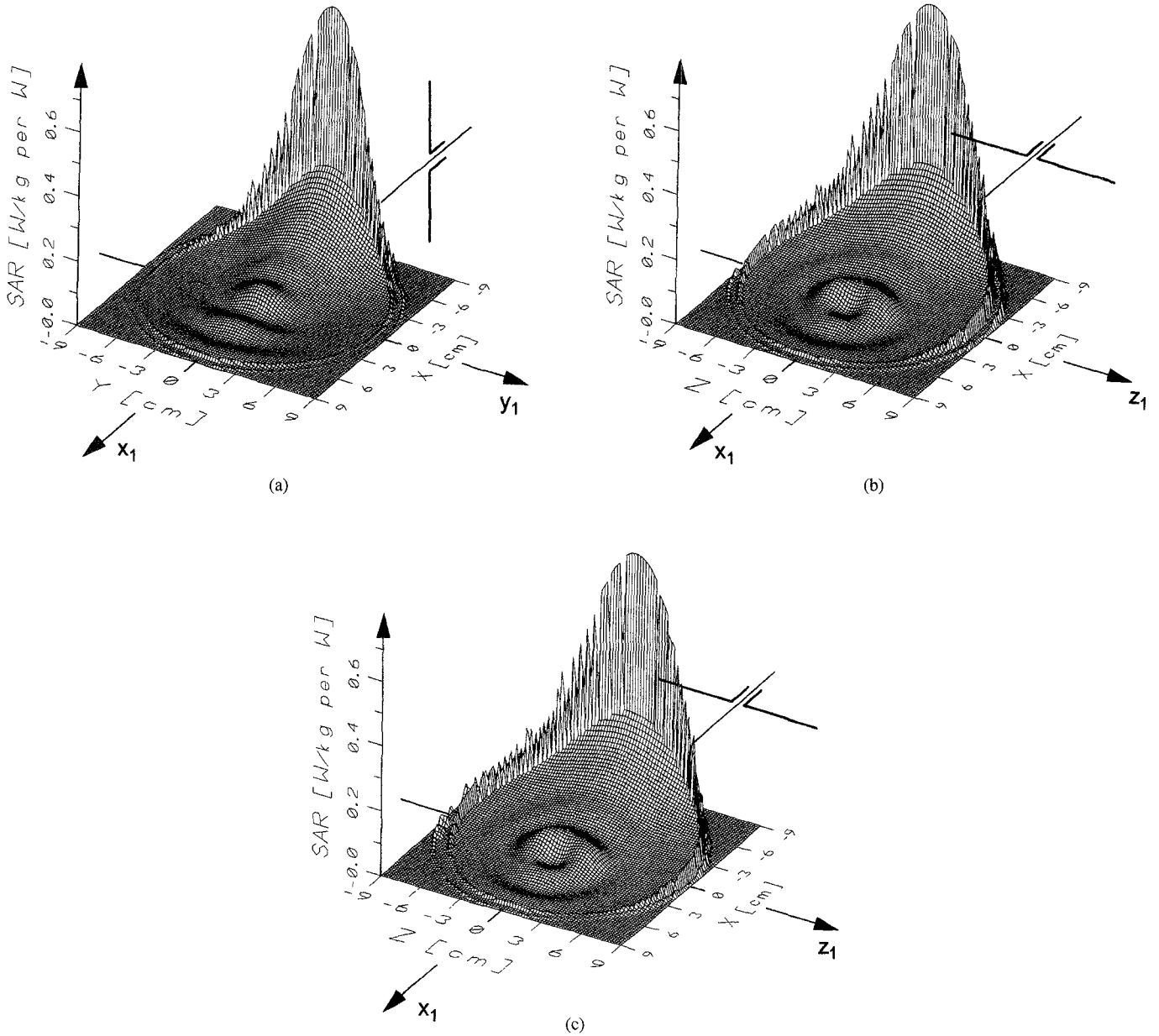

Fig. 5. SAR distribution in $x_1O_1y_1$ plane (a) and in $x_1O_1z_1$ plane (b), (c). Frequency $f = 0.9$ GHz; linear dipole antenna ($l = \lambda/2$, $\hat{e} = \hat{z}$) at $\phi_{inc} = 0°$, $\theta_{inc} = 90°$, $R = 17.5$ cm; spacing $R - \alpha_1 = 8.5$ cm; eccentricity $d = 0$ (a), (b) or $d = 4$ mm (c).

to the antenna. The peak SAR is 0.41 W/kg per W in the skin layer, 0.75 W/kg per W in the CSF layer, and 0.26 W/kg per W at the surface of the brain. There is also a secondary peak near the center of the brain ($x_1 = 3.6$ mm, $y_1 = z_1 = 0$): this central peak is an order of magnitude smaller than the superficial peaks and it may be attributed to focusing by the spherical cranial structure.

The effect of eccentricity can be seen in Fig. 5(c) which refers to the eccentric spheres model with eccentricity $d = 4$ mm. The SAR distribution in the coordinate plane $x_1O_1z_1$ is no longer symmetric with respect to the x_1- axis; it is possible to distinguish the weakly absorbing eccentric bone shell between the highly absorbing CSF and skin layers. The SAR distribution in the brain is practically identical to that of Fig. 5(b), though slightly shifted as a result of the brain displacement in the (eccentric) bone shell.

We conclude this numerical application with an investigation of the SAR distribution at 1.9 GHz (Fig. 6); the antenna-head separation is 4 cm. Fig. 6(a) and (b) display the SAR distribution in the coordinate planes $x_1O_1y_1$ and $x_1O_1z_1$, respectively, for the concentric spheres model. As a result of the decreased penetration depth, absorption is even more superficial at this frequency. The peak SAR is 5.6 W/kg per W in the skin layer, 4.1 W/kg per W in the CSF layer, and 1.5 W/kg per W at the surface of the brain, naturally on the side nearest to the antenna. Although the peak near the center of the brain appears quite weak at 1.9 GHz, it is actually comparable to the central peak observed at 0.9 GHz; the central peak is now located at $x_1 = 14.4$ mm, $y_1 = z_1 = 0$, which means that the focal point of the spherical cranial structure is farther away from the center of the brain at 1.9 GHz.

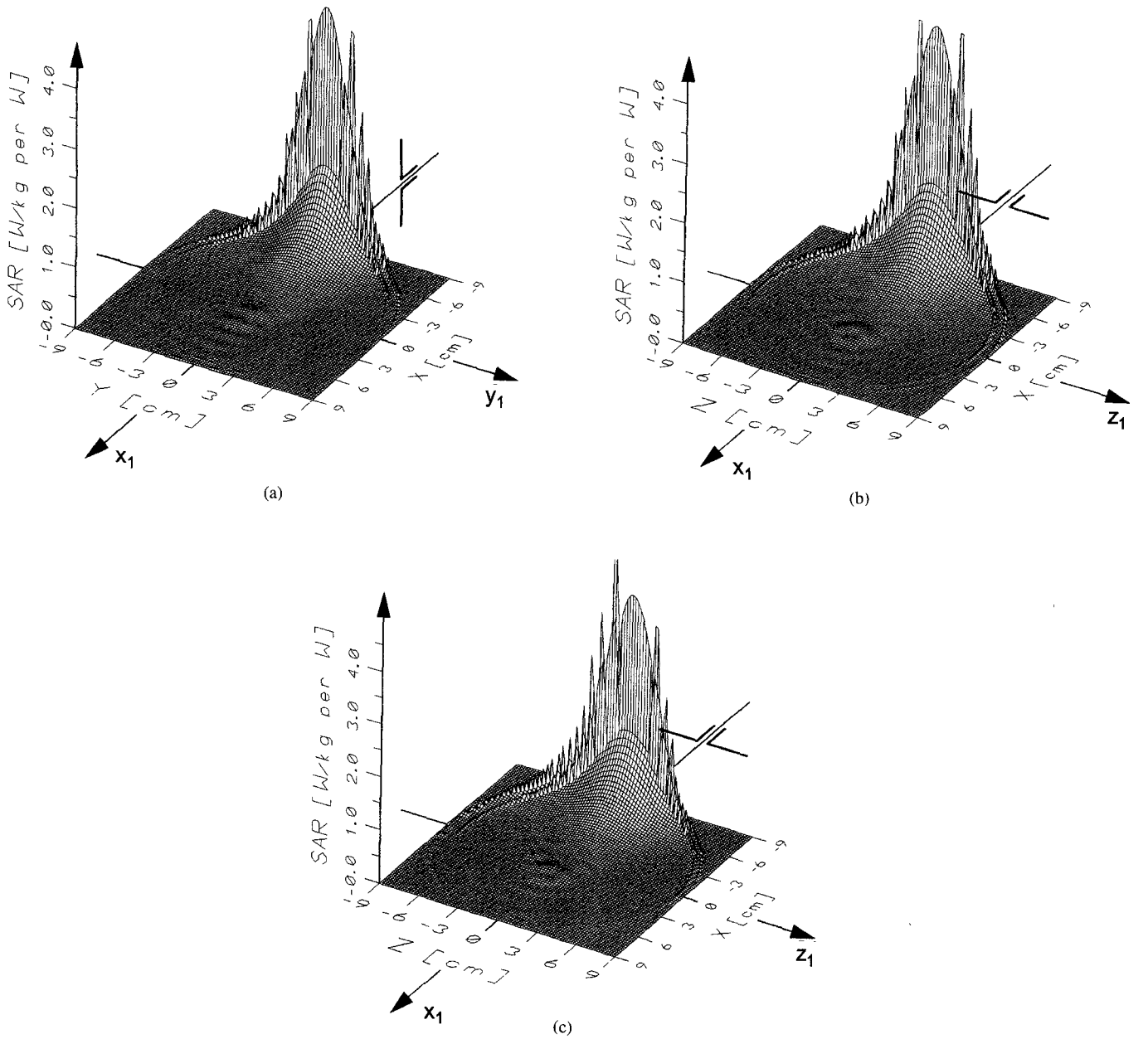

Fig. 6. SAR distribution in $x_1O_1y_1$ plane (a) and in $x_1O_1z_1$ plane (b), (c). Frequency $f = 1.9$ GHz; linear dipole antenna ($l = \lambda/2$, $\hat{e} = \hat{z}$) at $\phi_{inc} = 0°$, $\theta_{inc} = 90°$, $R = 13$ cm; spacing $R - \alpha_1 = 4$ cm; eccentricity $d = 0$ (a), (b) or $d = 4$ mm (c).

The effect of eccentricity can be realized by comparison of the SAR distributions in the coordinate plane $x_1O_1z_1$ for the concentric [Fig. 6(b)] and the eccentric [Fig. 6(c)] spheres models. The superficial SAR distribution on the side nearest to the antenna is distorted as a result of the geometrical asymmetry associated with nonzero eccentricity. The SAR distribution in the brain is practically unaffected by the eccentricity but, plausibly, it follows the displacement of the brain core within the eccentric bone shell.

As safety guidelines are usually given in terms of SAR averaged over 1 g of tissue, it is expedient to discuss the relevance of our results in terms of this dosimetric measure. The peak SAR averaged over 1 g of skin tissue is 0.37 W/kg per W at 0.9 GHz and 4.2 W/kg per W at 1.9 GHz; the superficial peaks in the brain, averaged over 1 g of tissue, are 0.21 W/kg per W at 0.9 GHz and 1.1 W/kg per W at 1.9 GHz. With regard to the ANSI-IEEE C95.1-1982 safety guide [1], the results of this model for the brain are well below the threshold (8 W/kg per W) at both frequencies. Our results for the skin are also below the threshold, although the peak at 1.9 GHz is above a proposed threshold (1.6 W/kg per W) for the general public. Comparisons with published numerical results [4], [5], and [7] indicate that the predictions of this model are in general somewhat higher, which suggests that our model may provide conservative estimates of the thermal load due to RF exposure.

VI. Concluding Remarks

The main contribution of this paper is the presentation of a concise analytical solution to the EM field induced in a

layered eccentric spheres structure. This exact solution can be used in conjunction with any time-harmonic localized source or a simple plane-wave excitation. The layered eccentric spheres model offers an extra degree of freedom to analytical investigations of EM absorption by the human head.

The numerical application provides specific information about the frequency-dependence of the total absorbed power, the role of individual layers in the absorption of the incident radiation, and the SAR distribution throughout the layered cranial structure. Eccentricity mainly manifests itself as a reduction of the total absorbed power and of the power absorbed in each layer, from the level corresponding to the concentric spheres model. Absorption is mostly superficial, especially at high frequencies; it is strongest on the side nearest to the antenna and it is weaker for larger antenna-head separation. The peak SAR averaged over 1 g of tissue in the brain is 0.21 W/kg per W at 0.9 GHz and 1.1 W/kg per W at 1.9 GHz; both values are below the threshold suggested by ANSI guidelines.

APPENDIX A
TRANSLATION OF VECTOR SPHERICAL HARMONICS

With regard to the triple-center geometry of Fig. 1(b), any field point may be represented by the position vectors $\vec{r}_1$, $\vec{r}_2 = \vec{r}_1 - d\hat{z}_1$, and $\vec{r} = R\hat{i} + \vec{r}_1$. The following transformation applies to the translation of vector spherical harmonics from O to O_1 [31] and [32]

$$\begin{bmatrix} \vec{M}_{mn}^{(i)}(k, \vec{r}) \\ \vec{N}_{mn}^{(i)}(k, \vec{r}) \end{bmatrix} = \sum_{\nu=1}^{\infty} \sum_{\mu=-\nu}^{\nu} \begin{bmatrix} A_{\mu\nu, \tilde{i}}^{mn} & B_{\mu\nu, \tilde{i}}^{mn} \\ B_{\mu\nu, \tilde{i}}^{m\tilde{n}} & A_{\mu\nu, \tilde{i}}^{m\tilde{n}} \end{bmatrix} \cdot \begin{bmatrix} \vec{M}_{\mu\nu}^{(\tilde{1})}(k, \vec{r}_1) \\ \vec{N}_{\mu\nu}^{(\tilde{1})}(k, \vec{r}_1) \end{bmatrix} \tag{A1}$$

under the constraint $r_1 \leq R$; if $r_1 \geq R$, subscripts and superscripts marked by a tilde must be interchanged in the right-hand side of (A1). The coupling coefficients $A_{\mu\nu, i}^{mn}$, $B_{\mu\nu, i}^{mn}$ are given by

$$A_{\mu\nu, i}^{mn} = (-1)^{\mu} \sum_{p} a(m, n| -\mu, \nu|p) a(n, \nu, p) z_p^{(i)}(kR) \cdot P_p^{m-\mu}[\cos(\pi - \theta_{inc})] e^{j(m-\mu)\phi_{inc}} \tag{A2a}$$

$$B_{\mu\nu, i}^{mn} = (-1)^{\mu} \sum_{p} a(m, n| -\mu, \nu|p+1, p) b(n, \nu, p+1) \cdot z_{p+1}^{(i)}(kR) P_{p+1}^{m-\mu}[\cos(\pi - \theta_{inc})] e^{j(m-\mu)\phi_{inc}} \tag{A2b}$$

and p is assigned the integers $|n-\nu|, |n-\nu|+2, \cdots, n+\nu$. Definitions for the various symbols used in (A2) can be found in [33].

The translation of vector spherical harmonics from O_2 to O_1 is performed as follows:

$$\begin{bmatrix} \vec{M}_{mn}^{(i)}(k, \vec{r}_2) \\ \vec{N}_{mn}^{(i)}(k, \vec{r}_2) \end{bmatrix} = \sum_{\nu=m'}^{\infty} \begin{bmatrix} A_{m\nu, \tilde{i}}^{mn} & B_{m\nu, \tilde{i}}^{mn} \\ B_{m\nu, \tilde{i}}^{m\tilde{n}} & A_{m\nu, \tilde{i}}^{m\tilde{n}} \end{bmatrix} \cdot \begin{bmatrix} \vec{M}_{m\nu}^{(\tilde{1})}(k, \vec{r}_1) \\ \vec{N}_{m\nu}^{(\tilde{1})}(k, \vec{r}_1) \end{bmatrix} \tag{A3}$$

The initial value of ν is $m' = \max\{1, |m|\}$. Equation (A3), as shown, applies for $r_1 \leq d$; if $r_1 \geq d$, subscripts and superscripts marked by a tilde must be interchanged in the right-hand side of (A3). The coupling coefficients $A_{m\nu, i}^{mn}$, $B_{m\nu, i}^{mn}$ are given by

$$A_{m\nu, i}^{mn} = (-1)^{m+n+\nu} \sum_{p} \alpha(m, n| -m, \nu|p) \cdot \alpha(n, \nu, p) z_p^{(i)}(kd) \tag{A4a}$$

$$B_{m\nu, i}^{mn} = -(-1)^{m+n+\nu} \sum_{p} \alpha(m, n| -m, \nu|p+1, p) \cdot b(n, \nu, p+1) z_{p+1}^{(i)}(kd), \tag{A4b}$$

REFERENCES

[1] O. P. Gandhi, Ed., *Biological Effects and Medical Applications of Electromagnetic Energy.* Englewood Cliffs, NJ: Prentice-Hall, 1990.

[2] M. A. Morgan, "Finite-element calculation of microwave absorption by the cranial structure," *IEEE Trans. Biomed. Eng.*, vol. BME-28, no. 10, pp. 687–695, Oct. 1981.

[3] P. J. Dimbylow and O. P. Gandhi, "Finite-difference time-domain calculations of SAR in a realistic heterogeneous model of the head for plane-wave exposure from 600 MHz to 3 GHz," *Phys. Med. Biol.*, vol. 36, no. 8, pp. 1075–1089, Aug. 1991.

[4] P. J. Dimbylow, "FDTD calculations of the SAR for a dipole closely coupled to the head at 900 MHz and 1.9 GHz," *Phys. Med. Biol.*, vol. 38, pp. 361–368, 1993.

[5] P. J. Dimbylow and S. M. Mann, "SAR calculations in an anatomically realistic model of the head for mobile communication transceivers at 900 MHz and 1.8 GHz," *Phys. Med. Biol.*, vol. 39, pp. 1537–1553, 1994.

[6] L. Martens, J. De Moerloose, D. De Zutter, J. De Poorter, and C. De Wagter, "Calculation of the electromagnetic fields induced in the head of an operator of a cordless telephone," *Radio Sci.*, vol. 30, no. 1, pp. 283–290, Jan./Feb. 1995.

[7] M. A. Jensen and Y. Rahmat-Samii, "EM interaction of handset antennas and a human in personal communications," *Proc. IEEE*, vol. 83, no. 1, pp. 7–17, Jan. 1995.

[8] A. R. Shapiro, R. F. Lutomirski, and H. T. Yura, "Induced fields and heating within a cranial structure irradiated by an electromagnetic plane wave," *IEEE Trans. Microwave Theory Tech.*, vol. MTT-19, no. 2, pp. 187–196, Feb. 1971

[9] W. T. Joines and R. J. Spiegel, "Resonance absorption of microwaves by the human skull," *IEEE Trans. Biomed. Eng.*, vol. BME-21, no. 1, pp. 46–48, Jan. 1974.

[10] A. Hizal and Y. K. Baykal, "Heat potential distribution in an inhomogeneous spherical model of a cranial structure exposed to microwaves due to loop or dipole antennas," *IEEE Trans. Microwave Theory Tech.*, vol. MTT-26, no. 8, pp. 607–612, Aug. 1978.

[11] J. W. H. Meijs and M. J. Peters, "The EEG and MEG, using a model of eccentric spheres to describe the head," *IEEE Trans. Biomed. Eng.*, vol. BME-34, no. 12, pp. 913–920, Dec. 1987.

[12] B. N. Cuffin, "Eccentric spheres models of the head," *IEEE Trans. Biomed. Eng.*, vol. BME-38, no. 9, pp. 871–878, Sept. 1991.

[13] N. C. Skaropoulos, M. P. Ioannidou, and D. P. Chrissoulidis, "Indirect mode matching solution to scattering from a dielectric sphere with an eccentric inclusion," *J. Opt. Soc. Am. A*, vol. 11, no. 6, pp. 1859–1866, June 1994.

[14] K. R. Foster and H. P. Schwan, "Dielectric properties of tissues," in *Handbook of Biological Effects of Electromagnetic Fields*, C. Polk and E. Postow, Eds Boca Raton, FL: CRC Press, 1986, pp. 27–96.

[15] P. M. Morse and H. Feshbach, *Methods of Theoretical Physics.* New York: McGraw-Hill, 1953, pt. II.

[16] M. Abramowitz and I. A. Stegun, *Handbook of Mathematical Functions.* New York: Dover, 1972.

[17] J. D. Jackson, *Classical Electrodynamics.* New York: Wiley, 1975.

[18] I. S. Gradshteyn and I. M. Ryzhik, *Table of Integrals, Series, and Products.* San Diego: Academic Press, 1980.

[19] K. R. Foster and J. L. Schepps, "Dielectric properties of tumor and normal tissues at radio through microwave frequencies," *J. Microwave Power*, vol. 16, no. 2, pp. 107–119, 1981.

[20] J. P. Grant, R. N. Clarke, G. T. Symm, and N. M. Spyrou, "*In vivo* dielectric properties of human skin from 50 MHz to 2.0 GHz," *Phys. Med. Biol.*, vol. 33, no. 5, pp. 607–612, 1988.

[21] T. Tamura, M. Tenhunen, T. Lahtinen, T. Repo, and H. P. Schwan, "Modeling of the dielectric properties of normal and irradiated skin," *Phys. Med. Biol.*, vol. 39, pp. 927–936, 1994.

[22] E. C. Burdette, F. L. Cain, and J. Seals, "*In vivo* probe measurement technique for determining dielectric properties at VHF through microwave frequencies," *IEEE Trans. Microwave Theory Tech.*, vol. MTT-28, no. 4, pp. 414–427, Apr. 1980.
[23] J. D. Kosterich, K. R. Foster, and S. R. Pollack, "Dielectric permittivity and electrical conductivity of fluid saturated bone," *IEEE Trans. Biomed. Eng.*, vol. BME-30, no. 2, pp. 81–86, Feb. 1983.
[24] H. P. Schwan, R. J. Sheppard, and E. H. Grant, "Compex permittivity of water at 25°C," *J. Chem. Phys.*, vol. 64, pp. 2257–2258, 1995.
[25] K. R. Foster, J. L. Shepps, R. D. Stoy, and H. P. Schwan, "Dielectric properties of brain tissue between 0.01 and 10 GHz," *Phys. Med. Biol.*, vol. 24, no. 6, pp. 1177–1187, June 1979.
[26] A. Krasziewski, A. Stuchly, M. A. Stuchly, and A. M. Smith, "*In vivo* and *in vitro* dielectric properties of animal tissues at radio frequencies," *Bioelectromagnetics,* vol. 3, pp. 421–433, 1982.
[27] N. R. V. Nightingale, V. D. Goodridge, R. J. Sheppard, and J. L. Christie, "The dielectric properties of the cerebellum, cerebrum and brain stem of mouse brain at radiowave and microwave frequencies," *Phys. Med. Biol.*, vol. 28, no. 8, pp. 897–903, Aug. 1983.
[28] M. Thurai, V. D. Goodridge, R. J. Sheppard, and E. H. Grant, "Variation with age of the dielectric properties of mouse brain cerebrum," *Phys. Med. Biol.*, vol. 29, no. 9, pp. 1133–1136, Sept. 1984.
[29] M. C. Steel and R. J. Sheppard, "Dielectric properties of mammalian brain tissue between 1 and 18 GHz," *Phys. Med. Biol.*, vol. 30, no. 7, pp. 621–630, July 1985.
[30] A. Ishimaru, *Wave Propagation and Scattering in Random Media.* New York: Academic Press, 1978.
[31] S. Stein, "Addition theorems for spherical wave functions," *Quart. Appl. Math.*, vol. 19, pp. 15–24, 1961.
[32] O. R. Cruzan, "Translational addition theorems for spherical vector wave functions," *Quart. Appl. Math.*, vol. 20, pp. 33–40, 1962.
[33] J. D. Kanellopoulos and J. G. Fikioris, "Resonant frequencies in an electromagnetic eccentric spherical cavity," *Quart. Appl. Math.*, vol. 37, pp. 51–66, 1979.

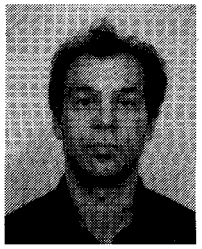

Nikos C. Skaropoulos (S'94) was born in Thessaloniki, Greece, in 1970. He received the M.Sc. degree in 1993 from the Department of Electrical and Computer Engineering, Faculty of Technology, Aristotle University of Thessaloniki, Greece. He is working toward the Ph.D. degree at the same university.

He is presently a Research and Teaching Assistant of the above institution. His research interests are in the biological effects of electromagnetic waves and in wave propagation and scattering in random media.

Mr. Skaropoulos is a member of the Technical Chamber of Greece.

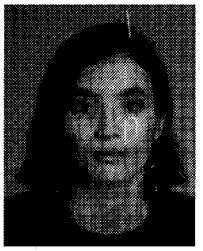

Melina P. Ioannidou (S'94) was born in Thessaloniki, Greece, in 1964. She received the M.Sc. degree in 1989 from the Department of Electrical and Computer Engineering, Faculty of Technology, Aristotle University of Thessaloniki, Greece. She is currently working toward the Ph.D. degree at the same university.

She is currently a Research and Teaching Assistant of the above institution. Her research interests are in propagation and scattering of electromagnetic waves and in radar meteorology.

Ms. Ioannidou is a member of the Technical Chamber of Greece.

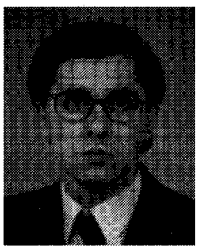

Dimitris P. Chrissoulidis (S'79–M'84) was born in Thessaloniki, Greece, in 1956. He received the M.Sc. degree in 1979 and the Ph.D. degree in 1984, both from the Department of Electrical and Computer Engineering, Faculty of Technology, Aristotle University of Thessaloniki, Greece.

He is currently an Associate Professor of the aforementioned institution. During the academic year 1988 to 1989, he was a Postdoctoral Fellow of the Royal Norwegian Council for Scientific and Industrial Research, Kjeller, Norway. His research interests include propagation and scattering of electromagnetic waves, active remote sensing of the environment and underwater acoustics. He authored or coauthored several journals papers. He is coauthor of the book *Electromagnetics and Optics* (World Scientific, 1992).

Dr. Chrissoulidis is a member of the AGU, URSI-F, and of the Technical Chamber of Greece.